Developing a Digital Twin Framework for Wind Tunnel Testing: Validation of Turbulent Inflow and Airfoil Load Applications

Rishabh Mishra[1], Emmanuel Guilmineau[1], Ingrid Neunaber[2], and Caroline Braud[1]

[1]LHEEA lab. - CNRS - Nantes Université, Centrale Nantes, 1 rue de la Noë, 44100 Nantes.
[2]NTNU, Høgskoleringen 1, 7034 Trondheim, Norway

Correspondence: Rishabh Mishra (rishabh.mishra@ec-nantes.fr)

Abstract. Wind energy systems, such as horizontal-axis wind turbines and vertical-axis wind turbines, operate within the turbulent atmospheric boundary layer, where turbulence significantly impacts their efficiency. Therefore, it is crucial to investigate the impact of turbulent inflow on the aerodynamic performance at the rotor blade scale. As field investigations are challenging, in this work, we present a framework where we combine wind tunnel measurements in turbulent flow with a digital twin of the experimental setup. For this, first, the decay of the turbulent inflow needs to be described and simulated correctly. Here, we use Reynolds-Averaged Navier-Stokes (RANS) simulations with $k-\omega$ turbulence models, where a suitable turbulence length scale is required as an inlet boundary condition. While the integral length scale is often chosen without a theoretical basis, this study derives that the Taylor micro-scale is the correct choice for simulating regular grid generated turbulence: the temporal decay of turbulent kinetic energy (TKE) is shown to depend on the initial value of the Taylor micro-scale by solving the differential equations given by Speziale and Bernard (1992). Further, the spatial decay of TKE and its dependence on the Taylor micro-scale at the inlet boundary are derived. With this theoretical understanding, RANS simulations with $k-\omega$ turbulence models are conducted using the Taylor micro-scale and the TKE obtained from grid experiments as the inlet boundary condition. Second, the results are validated with excellent agreement with the TKE evolution downstream of a grid obtained through hot-wire measurements in the wind tunnel. Third, the study further introduces an airfoil in both the experimental and the numerical setting where 3d simulations are performed. A very good match between force coefficients, obtained in experiments and in the digital twin, is found. In conclusion, this study demonstrates that the Taylor micro-scale is the appropriate turbulence length scale to be used as the boundary condition and initial condition to simulate the evolution of TKE for regular grid generated turbulent flows. Additionally, the digital twin of the wind tunnel can accurately replicate the force coefficients obtained in the physical wind tunnel.

1 Introduction

Wind energy systems, such as horizontal-axis and vertical-axis wind turbines, operate in a turbulent atmospheric boundary layer, which significantly affects their efficiency. Therefore, it is essential to study the turbulent inflow that they encounter. Important statistical quantities that considerably affect the aerodynamic performance of a rotor blade are the turbulent kinetic energy (TKE) and length scales in the wind. To study their effects, field experiments can be carried out, but they are complex,

time-consuming, and costly. Alternatively, experiments can be conducted in a wind tunnel by subjecting a Reynolds-scaled wind turbine rotor or a blade section from a real wind turbine blade to turbulent inflow under different inflow conditions, such as homogeneous inflow or gust inflow (see e.g., Wei et al. (2019); Wester et al. (2022); Mishra et al. (2022); Nietiedt et al. (2022) and Neunaber and Braud (2020a)). However, wind turbines have grown to become the largest flexible, rotating machines in the world, with blade lengths approaching now 120m. The interaction between a highly variable inflow and the unsteady aerodynamics of the moving and deforming blades is pushing the limits of current theory Veers et al. (2019). At the blade scale, chord-based Reynolds numbers will exceed 15 millions, which is unreachable in most available wind tunnels, and reach limits of pressurised facilities that are specifically developed for that purpose (Miller et al., 2019; Brunner et al., 2021). Therefore, having a digital twin model is a key to help in the development of very large horizontal axis wind turbines (HAWT). Indeed, with these digital twin models, aerodynamic loads from local blade sections, used as input of Blade Element Momentum (BEM) solvers, can be pushed towards very large Reynolds numbers in numerous configurations encountered locally by blade sections (due to elasticity and floating movements). This would also provide the full flow and load description to understand further unsteady aerodynamics of blades in such configurations and thus further improve blade design of very large HAWT. Among the Computational Fluid Dynamics (CFD) methods available for that purpose, a Reynolds Average Navier-Stokes (RANS) formulation will be preferred over solving the Navier Stokes Equations directly with numerical methods using Direct Numerical Simulation (DNS) or Large Eddy Simulation (LES), as it is computationally too expensive for the targeted system. However, many challenges still remain and some of them will be tackled in this paper at low Reynolds number as a first step to be able to provide experimental validation. It concerns:

1. The theoretical description of the decay properties of turbulence measures such as the TKE and the dissipation rate in the downstream flow direction, and

2. The numerical replication of the decay properties of turbulence measures such as the TKE and the dissipation rate in the downstream flow direction, and

3. The reproduction of the aerodynamic loads acting on an airfoil by means of RANS simulations.

The literature review is therefore split into three sub-sections to give the reader an overview over decaying turbulence, focusing on the known turbulent flow properties behind grids, the great effort made in the literature to replicate these properties on simulated flows, and the impact of turbulence on the aerodynamics of an airfoil.

Brief theoretical description of decaying grid turbulence

The Navier-Stokes equations are highly nonlinear and their solutions are non-unique in nature. Therefore, simplifications are often made when describing or simulating turbulent flows, and here, we focus on literature on grid generated turbulence (GDT). Over the decades, GDT has been investigated intensely, and different works looked into the empirical and analytical description of the evolution of the turbulence decay. According to Batchelor and Townsend (1948), the decay of the turbulence intensity can be described by means of a power law. It has further been discussed that the inlet conditions play a role in the decay of

the turbulence (Kurian and Fransson (2009)). The works of Comte-Bellot and Corrsin (1966) show experimentally that the ratio between TKE and dissipation evolve linearly in the downstream direction. A literature review can be found in Kurian and Fransson (2009). We will use the existing framework that was very briefly summarized above as a starting point for our

60 theoretical framework, and a detailed description of both is given in section 2.

Simulating decaying grid turbulence

Simulating the inflow environment using computational fluid mechanics (CFD) has been the subject of many research works, and different turbulent formulations can be used that are summarized below from the most expensive computational effort to the least one, i.e., RANS models.

65 Nagata et al. (2008) performed DNS to simulate the turbulence mixing layer for grid-generated turbulence, and they replicated typical GDT including the shear mixing layer. Continuing this work, Suzuki et al. (2010) showed that for a given mesh Reynolds number (Re_M), turbulence mixing is enhanced for fractal grids compared to regular grids. Laizet and Vassilicos (2011) simulated both a regular and different fractal grids using DNS, and they confirm the characteristic regions of turbulence production and decay downstream of fractal grids. Continuing their work, Laizet et al. (2013) studied inter-scale energy transfer

70 of decaying turbulence for fractal grids. Efforts have also been made to use LES to simulate GDT. For example, Blackmore et al. (2013) developed a grid inlet technique to generate high intensity turbulence for given length scales in LES simulations. With this, they successfully imitated the independence of the decay rate of the turbulence intensity (TI) from the mesh-size-based Reynolds number Re_M. Rieth et al. (2014) compared two LES models, namely the sigma model (see Nicoud et al. (2011)) and the Smagorinsky model (see, Smagorinsky (1963)), to simulate grid generated turbulence. They found that the sigma model

75 is a good alternative to the static Smagorinky model and comparable to the dynamic Smagorinky model (see Germano et al. (1991)). Further, Liu et al. (2017) employed 3d LES to simulate GDT, and they found the same trend of absolute values of the mean TI. Djenidi (2006) used a Lattice Boltzmann method to simulate GDT, and he managed to simulate the decay power law over a short distance from the grid but found it difficult to find the decay exponent.

Finally, Torrano et al. (2015) have investigated the performance of various two-equation eddy viscosity models for predicting

80 the decay of the turbulent kinetic energy downstream of a regular grid by means of RANS. They calculated the dissipation rate using an integral length scale equal to the grid mesh size. The simulation results were compared with experimental results, and a conclusion of their work was that eddy viscosity models were over-predicting the turbulent kinetic energy in comparison to the experiments. As an alternative to two-equation eddy viscosity models, Reynolds stress transport models (RSTM) can also be used where transport equations for each of the Reynolds stress terms are solved. For example, Panda et al. (2018)

85 performed RANS simulations using RSTM. However, because of the closure problem, using RSTM is quite complex as the nine non-closed components of the nine Reynolds stress transport equations have to be modeled.

Regarding RANS equations, studies focus mostly on improving the eddy viscous model, while not much effort was put on the choice of the length scale that is usually assumed to have an order of magnitude of the integral length scale. Two quantities are generally used at the inlet of RANS simulations: the turbulence intensity and the length scale. Indeed, when using the most

90 popular two-equation eddy viscosity models, namely the $k - \epsilon$ and $k - \omega$ models Wilcox (1988), or a mixture of these two

models, the $k - \omega$ SST Menter 1994 and 2003 models (Menter (1994), Menter et al. (2003)), the following quantities need to be provided at the inlet boundary: k, the turbulent kinetic energy, ϵ, the dissipation rate, and ω, the specific dissipation rate. k is generally given through a turbulence intensity quantity, and ϵ and ω are computed using k and a given characteristic turbulence length scale chosen individually for each flow configuration. For example, in the case of pipe flow, the turbulence length scale

95   is empirically approximated as 0.07 times the diameter of the pipe (Versteeg and Malalasekera (1995)).

We would like to emphasize that a correctly evaluated and properly defined turbulence length scale is a basic requirement to accurately capture the evolution of turbulence. Finally, in principle, if provided with a perfect closure, the RANS model should be able to capture statistical measures of turbulence and their evolution in the flow field. The present work will focus on improving the length scale choice to reproduce the correct evolution of k.

100

Experimental and numerical aerodynamic research

As stated above, the third challenge of the work presented here is the reproduction of aerodynamic loads on a 2d airfoil section by means of RANS simulations in particular for low Reynolds numbers. There are many experimental works that describe the evolution of the lift and drag coefficients with the variation of the angle of attack (AoA) of the airfoil, and a summary of the

105   design and aerodynamics for wind turbine blades can for example be found in Bak (2022). For this work, the impact of low Reynolds numbers and the impact of turbulence on the performance of 2d blade sections is of interest. Different studies on the influence of the turbulence intensity in the inflow on the aerodynamics of a 2d blade section are summarized in Li and Hearst (2021). There, an NREL S826 profile is exposed to different turbulence levels up to 5.4% for a chord-based Reynolds number of $Re_c = 4 \cdot 10^5$ defined as $Re_c = \frac{c \cdot U_\infty}{\nu}$, where c denotes the chord length, U_∞ denotes the inflow velocity, and ν the kine-

110   matic viscosity. They found that the slope of linear part of the lift curve increases with increasing turbulence intensity and that turbulence intensities of up to 1.6% led to a reduction of the maximum lift whereas turbulence intensities of 2.1% and higher led to an increase in lift compared to the reference case. Devinant et al. (2002) and Sicot et al. (2006) studied the influence of turbulence intensities up to 16% on the aerodynamics of a 2d NACA65(4)421 blade section. The chord-based Reynolds numbers were $1 \cdot 10^5 \leq Re_c \leq 7 \cdot 10^5$. Devinant et al. (2002) showed that increasing the turbulence intensity shifts the stall angle

115   towards higher angles of attack. This is attributed to a turbulent boundary layer flow that is known to be less prompt to flow separation, which also displaces the transition towards the trailing edge. Sicot et al. (2006) found that the fluctuations of the surface pressure measurements, characterized by the standard deviation, increased in the separated flow region with increasing turbulence intensity. The average location of the separation line was not affected.

Simulating turbulent flow upstream of the airfoil often requires the use of LES, as demonstrated in the work by Gilling et al.

120   (2009). In this paper, we will show that with appropriate boundary conditions at the inlet, RANS simulations can yield accurate evolution of turbulence properties.

Fewer investigations of the impact of turbulence have been performed at higher Reynolds numbers due to experimental complexity. The present digital-twin model will pave the way for such studies.

Structure of this paper

125   As stated above, the aim of this work is the creation a digital-twin of a low-Reynolds number wind tunnel where turbulence is generated with grids. For this, first, a theoretical framework is developed in section 2 to demonstrate that the Taylor micro-scale (λ) is the correct length scale to be used as the turbulence length scale in RANS simulations for homogeneous, isotropic turbulent flows. Additionally, we show that the spatial and temporal decays of turbulent kinetic energy are directly dependent on the Taylor micro-scale, and we derive a relation between the Taylor micro-scale and the downstream position. In section

130   3, the theoretical framework is then validated using RANS simulations and experiments behind a homogeneous grid; the experimental and numerical set-ups are detailed in sections 3.1 and 3.2. A validation and the results are presented in section 3.4. In the next step, the digital twin is used to perform aerodynamic simulations which are compared to experiments. The numerical and experimental setups are explained in sections 4.2 and 4.1, and the results are compared in section 4.3. Finally, conclusions and perspectives are given in section 5.

135   **2   Theoretical framework**

In the following, we will detail on the theoretical framework of the decay of homogeneous, isotropic turbulence that will lay the foundation of our digital twin. We will start with some important equations from literature and develop them further.

2.1   Dependence of the temporal evolution of k on λ

Researchers in the physics and mathematics community have studied the case of homogeneous isotropic turbulence in great

140   detail. Batchelor and Townsend (1948) proposed to call the Reynolds number based on the Taylor micro-scale (λ) the "Reynolds number of turbulence", and also suggested that λ is representative of the eddies of large wave-number, i.e., small eddies. In the theory of homogeneous isotropic turbulence, it is necessary to assume the similarity of turbulence at all stages of decay, i.e., changes in the structure of turbulence can be described by two parameters, namely a characteristic length and a characteristic velocity (see Stewart and Townsend (1951)). Later on, George (1992) proved that the characteristic length scale of the entire

145   energy spectrum is the Taylor micro-scale. This is confirmed by Speziale and Bernard (1992), who also proposed that the turbulent kinetic energy and the Taylor micro-scale are the appropriate scaling parameters for all scales of motion. They proposed a set of differential equations to calculate the temporal decay of turbulent kinetic energy, $k(t)$, and dissipation rate, $\epsilon(t)$:

$$\frac{dk(t)}{dt} = \epsilon(t), \tag{1}$$

150   $$\frac{d\epsilon(t)}{dt} = -\alpha \frac{\epsilon(t)^2}{k(t)}. \tag{2}$$

Here, α is a constant. Equations (1) and (2) formulate an initial value problem which can easily be solved to give a temporal decay law for initial conditions at time $t = 0$, $k(t) = k(0)$ and $\epsilon(t) = \epsilon(0)$ (cf. Zhou and Speziale (1998)), which gives

$$k(t) = k(0) \left(1 + \frac{1}{\alpha} \frac{\epsilon(0)}{k(0)} t \right)^{-\alpha}. \tag{3}$$

With the equation from Bailly and Comte-Bellot (2015),

155 $$\frac{k(0)}{\epsilon(0)} = \frac{(\lambda(0))^2}{20\nu}, \tag{4}$$

we can write equation (3) as

$$k(t) = k(0) \left(1 + \frac{1}{\alpha} \frac{20\nu}{(\lambda(0))^2} t \right)^{-\alpha}. \tag{5}$$

Looking at equation (5), we can clearly say that the temporal decay of the turbulent kinetic energy has a direct dependence on the initial Taylor micro-scale $\lambda(0)$. This is comforted by Mydlarski and Warhaft (1996) who empirically found a relationship

160 between the energy decay exponent and the Taylor Reynolds number R_λ.

2.2 Dependence of the spatial evolution of k on λ

The dependence of the downstream evolution of k on λ is demonstrated here within the framework of homogeneous, isotropic turbulence. For the steady-state case, the transport equation for k can be written as (here, we follow Einstein's summation

165 convention):

$$U_j \frac{\partial k}{\partial x_j} = \frac{\partial}{\partial x_j} \left(\frac{1}{\rho} \overline{u_j p} + \frac{1}{2} \overline{u_i u_i u_j} - 2\nu \overline{u_i s_{ij}} \right) - \overline{u_i u_j} S_{ij} - \epsilon. \tag{6}$$

U_j and u_j are the mean velocity and the velocity fluctuation, respectively, with $i, j = 1, 2, 3$. The pressure fluctuations are denoted by p, and ν is the kinematic viscosity of the fluid. s_{ij} is the strain rate tensor for velocity fluctuations, and S_{ij} is the strain rate tensor for the mean flow, defined as

170 $$S_{ij} = \frac{1}{2} \left(\frac{\partial U_i}{\partial x_j} + \frac{\partial U_j}{\partial x_i} \right), \tag{7}$$

$$s_{ij} = \frac{1}{2} \left(\frac{\partial u_i}{\partial x_j} + \frac{\partial u_j}{\partial x_i} \right). \tag{8}$$

The turbulent kinetic energy is defined as

$$k = \frac{1}{2} (\overline{u_1^2} + \overline{u_2^2} + \overline{u_3^2}). \tag{9}$$

It should be noted that for grid-generated turbulence

$$\overline{u_1^2} = 1.2\overline{u_2^2} = 1.2\overline{u_3^2} = \overline{u^2} \qquad (10)$$

is found (cf. Comte-Bellot and Corrsin (1966) and Bailly and Comte-Bellot (2015)).

After substituting (10) in (9), we get

$$k = \frac{4}{3}\overline{u^2}. \qquad (11)$$

If the dominant flow direction is the x_1 direction, then equation (6) can be written as

$$U_1 \frac{\partial k}{\partial x_1} = \underbrace{\frac{\partial}{\partial x_1} \left(\frac{1}{\rho}\overline{u_1 p} + \frac{1}{2}\overline{u_i u_i u_1} - 2\nu\overline{u_i s_{i1}} \right)}_{transport} - \underbrace{\overline{u_i u_1} S_{i1}}_{production} - \epsilon. \qquad (12)$$

If we assume the turbulence to be homogeneous and decaying, then the term representing the transport of k in an inhomogeneous field due to pressure fluctuation, the turbulence itself, and viscous stresses, and the term representing the production of k can be set to zero (see Bailly and Comte-Bellot (2015)).

Therefore, equation (12) becomes

$$\frac{\partial k}{\partial x} = -\epsilon/U. \qquad (13)$$

Here, we have dropped the indices for the sake of simplification. For homogeneous, isotropic turbulence, the dissipation rate ϵ can be related to both the longitudinal Taylor micro-scale (λ_1) and the transverse Taylor micro-scale (λ_2) as

$$\epsilon = 15\nu\frac{\overline{u^2}}{\lambda_2^2} = 30\nu\frac{\overline{u^2}}{\lambda_1^2}. \qquad (14)$$

By using equation (11), we can write equation (15) as

$$\epsilon = 11.25\nu\frac{k}{\lambda_2^2} = 22.5\nu\frac{k}{\lambda_1^2}. \qquad (15)$$

From here onwards, we will only use the relation corresponding to λ_1, and for simplicity, we will drop the subscript '1'. Hence, the relation for the dissipation rate ϵ can be written as

$$\epsilon = 22.5\nu\frac{k}{\lambda^2}. \qquad (16)$$

By substituting ϵ from equation (16) into equation (13), we arrive at

$$\frac{\partial k}{\partial x} = -\frac{22.5\nu}{U}\frac{k}{\lambda^2}. \tag{17}$$

Since the evolution of k is only a function of x, for the given case, the partial differential equation (PDE) (17) becomes an ordinary differential equation,

$$\frac{dk}{dx} = -\frac{22.5\nu}{U}\frac{k}{\lambda^2}. \tag{18}$$

Solving the differential equation (18),

$$k(x) = C_1 exp\left(-\frac{22.5\nu}{U}\int \frac{1}{\lambda^2}\,dx\right). \tag{19}$$

Equation (19) shows that the evolution of k in the downstream direction has a direct dependence on the Taylor micro-scale λ. Here, C_1 is a constant.

To find the final solution, we need to understand the dependence of λ on x. This is performed in the following section.

2.3 Dependence of λ on x

From equation (16) we know that $\lambda^2 \propto k/\epsilon$. Experiments have shown that for homogeneous isotropic turbulence, k/ϵ evolves linearly in the downstream direction (e.g., Comte-Bellot and Corrsin (1966)). Thus, we can write

$$\frac{k}{\epsilon} = \frac{k_{in}}{\epsilon_{in}} + \frac{m}{U}x, \tag{20}$$

where m/U is the slope. Now, using equations (16) and (20), we can write

$$\lambda^2 = 22.5\nu\left(\frac{k}{\epsilon}\right) = 22.5\nu\left(\frac{k_{in}}{\epsilon_{in}} + \frac{m}{U}x\right). \tag{21}$$

k_{in} and ϵ_{in} are the values of the turbulent kinetic energy and the dissipation rate at the inlet boundary. Substituting equation (21) into equation (19), performing integration, and subjecting it to the boundary condition at the inlet, $k(x=0) = k_{in}$, gives

$$k(x) = k_{in}\left(1 + m\frac{\epsilon_{in}}{k_{in}}\frac{x}{U}\right)^{-1/m}. \tag{22}$$

Using relation (16), we can rewrite equation (22) as

$$k(x) = k_{in}\left(1 + m\frac{22.5\nu}{\lambda_{in}^2}\frac{x}{U}\right)^{-1/m}, \tag{23}$$

were $\lambda(x = 0) = \lambda_{in}$. Looking at equation (23), we can say that the evolution of k in the downstream direction can be defined for a homogeneous, isotropic flow, provided we have the values of k_{in} and λ_{in} at the inlet.

From the framework of $k - \omega$ series of models for RANS simulations, one can also derive the following evolution equation for k for decaying, homogeneous, isotropic turbulence (cf., Eça et al. (2016)),

$$k(x) = k_{in} \left(1 + \omega_{in}\beta\frac{x}{U}\right)^{-\beta^*/\beta}, \tag{24}$$

where ω is the so-called turbulence frequency that is related to ϵ and k by

$$\omega = \frac{\epsilon}{\beta^* k}, \tag{25}$$

and β and β^* are constants with values 0.0828 and 0.09 respectively (see Wilcox (1988)). The value of ω at the inlet boundary is given by ω_{in}. By substituting equation (25) into equation (24), we have

$$k(x) = k_{in} \left(1 + \frac{\beta}{\beta^*}\frac{\epsilon_{in}}{k_{in}}\frac{x}{U}\right)^{-\beta^*/\beta}. \tag{26}$$

Using relation (16), we can rewrite equation (27) as following,

$$k(x) = k_{in} \left(1 + \frac{\beta}{\beta^*}\frac{22.5\nu}{\lambda_{in}^2}\frac{x}{U}\right)^{-\beta^*/\beta}. \tag{27}$$

Equations (23) and (27) have a similar form. Even if the equation (27) comes from the $k - \omega$ model, believing in its proven applicability, we can assume that,

$$m = \frac{\beta}{\beta^*}. \tag{28}$$

Therefore, the value of m can be taken as 0.92. It is important to notice that further investigations are required to find the correct value of the parameter m theoretically. For the cases where the assumption of Taylor's hypothesis is valid, i.e., time t equals x/U, the spatial evolution equation of k, equation (23), becomes equivalent to the temporal decay equation of k, cf. equation (5). Hence, measurements of k and λ at a given position in a homogeneous isotropic turbulent flow will enable us to obtain the evolution of k when solving the RANS equations. This is essential to reproduce realistic homogeneous, isotropic turbulent inflow conditions at the inlet boundary of RANS simulations. The experimental and numerical setups used to validate the spatial evolution equation (23) are presented in the following section.

3   Digital twin: simulating regular grid inflow in the wind tunnel

In the following, k and λ will be measured from the flow behind a grid in a wind tunnel facility. The objective is to demonstrate that the evolution of k obtained from RANS simulations matches the experiments when using k and λ from measurements at a given location. The wind tunnel facility and the grid set-up are described below together with the RANS simulations performed.
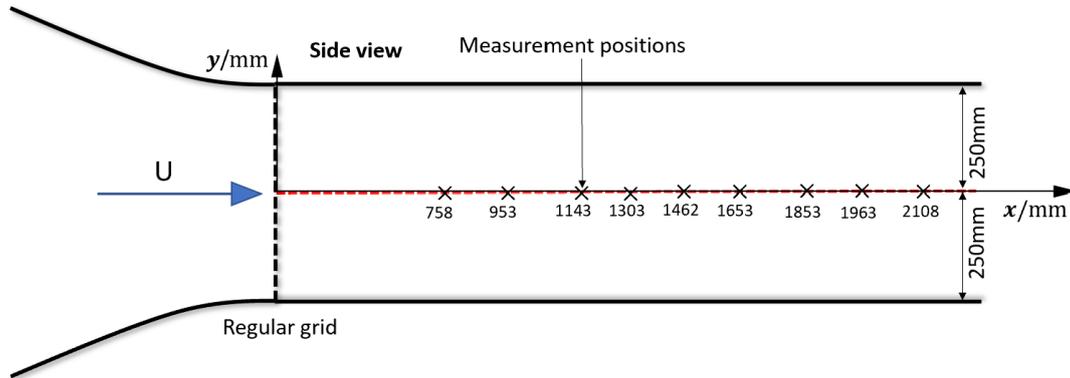
Figure 1. Schematic diagram of the experimental setup for hot-wire measurements in the wake of a regular grid (side view). The measurement positions are marked.

3.1 Experimental setup

The experiments were performed in the aerodynamic closed loop low-Reynolds number wind tunnel facility at the LHEEA (Laboratoire de recherche en Hydrodynamique, Énergetique et Environnment Atmospheric) laboratory of CNRS and Centrale Nantes (see figure 1). This wind tunnel has a cross-section of 0.5m × 0.5m and a test section length of 2.3m with a maximum inflow velocity of 40ms^{-1} and a turbulence intensity of less than 0.3%.

To induce a turbulent inflow, a regular wooden grid with square bars was used. The cross-section of the bars used for the frame is 11mm × 10.5mm and of the ones used for creating the mesh d = 6mm × 6mm. The blockage (b) of the grid is 16% and the mesh size M is 70mm × 70mm.

To measure the downstream evolution of turbulence properties of the inflow, a 1D hot-wire probe of type 55P11 with a wire length of 1.25mm from Dantec Dynamics was used. It was operated using a DISA55M01 unit. The hot-wire was calibrated in the velocity range $0.5\text{ms}^{-1} \leq U \leq 40\text{ms}^{-1}$ applying the temperature correction suggested by Hultmark and Smits (2010). During the measurements, the mean velocity was approximately 25ms^{-1}. The data was recorded at a sampling frequency of 25kHz for 10 seconds for calibration and 20 seconds for the measurements. A hardware low-pass filter with a cut-off frequency of 10kHz was used. The downstream evolution of k was measured at the centre-line of the wind tunnel at nine downstream positions that are indicated in figure 1.

3.2 Numerical setup

The simulations are performed using the finite volume based ISIS-CFD incompressible URANS solver. This solver, developed by CNRS and Centrale Nantes, also available as a part of the FINE™/Marine computing suite worldwide distributed by Cadence Design Systems, uses an incompressible unsteady Reynolds-averaged Navier-Stokes (URANS) method. The solver is based on a finite volume method to build the spatial discretization of the transport equations. The unstructured discretization is face-based, which means that cells with an arbitrary number of arbitrarily shaped faces are accepted. A second order backward
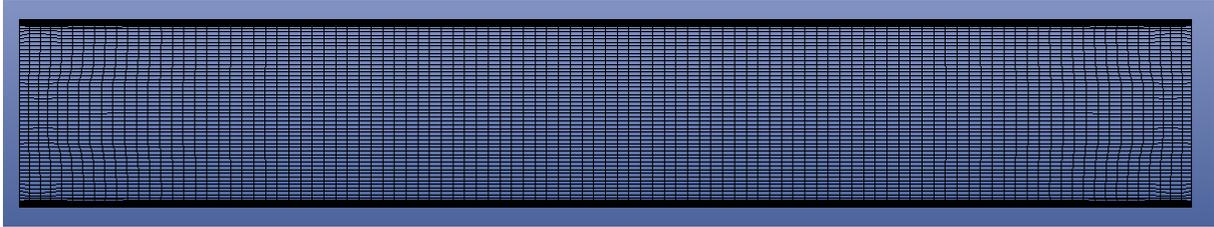
Figure 2. Simulation domain for decaying turbulence.

difference scheme is used to discretise time. All flow variables are stored at the geometric center of arbitrarily shaped cells. Volume and surface integrals are evaluated with second-order accurate approximations. As the method is face-based, numerical fluxes are reconstructed on the mesh faces by linear extrapolation of the integrand from the neighbouring cell centers. A centered scheme is used for the diffusion terms, whereas for the convective fluxes, a blended scheme with 80% central and 20% upwind is used. In the case of turbulent flows, additional transport equations for the variables in the turbulence model are added.

2d simulations are performed for the domain, mimicking the wind tunnel shown in figure 2, with a domain length of 3.12m, a width of 0.5m (same as the width of the wind tunnel test section), and 8000 cells. Simulations were performed with a higher number of cells (10000 and 12000) as well, but no changes were observed. The top and the bottom walls in the simulations were put to the no-slip condition.

It should be noted that the values put as the boundary condition at the inlet boundary are the ones obtained at the first point of the measurement, 758mm downstream of the inlet in the wind tunnel which refers to $x/M = 11$ in figures 4 and 5.

3.3 Length scales

For homogeneous, isotropic turbulence, both the integral length (L) and λ can be easily estimated using the one-dimensional energy spectrum (see Hinze (1975)). L can be obtained by taking the limit of the energy spectrum $E(f)$ in the frequency domain for $f \rightarrow 0$,

$$L = \lim_{f \to 0} \left(\frac{E(f) \cdot U}{4\sigma^2} \right). \tag{29}$$

Here, U is the mean streamwise velocity, u denotes the fluctuations, and σ is the standard deviation of the velocity time-series $U(t)$. It should be noticed that here, only the frequency range where $E(f) \approx const$ just outside of the inertial sub-range is used to determine L.

λ is defined as following,

$$\lambda = \left(\frac{\sigma^2}{\langle (\frac{\partial u}{\partial x})^2 \rangle} \right)^{1/2}, \tag{30}$$

where $\langle (\frac{\partial u}{\partial x})^2 \rangle$ can be estimated from the spectrum in the wave-number (κ) domain,

$$\left\langle \left(\frac{\partial u}{\partial x} \right)^2 \right\rangle = \int_{\kappa_{min}}^{\kappa_{max}} \kappa^2 E(\kappa) \, d\kappa, \tag{31}$$

where κ_{min} and κ_{max} are the wave number boundaries of the whole energy spectrum. At the downstream position $x/M = 11$, which represents the first point of measurement in the wind tunnel, we calculated L/M, λ/M, and the Taylor Reynolds number (Re_λ) using hot-wire measurements and equations (29) and (30). An exemplary spectrum is shown in figure 3. The calculated values were $L/M = 0.39$, $\lambda/M = 0.034$, and $Re_\lambda = 180$, respectively.
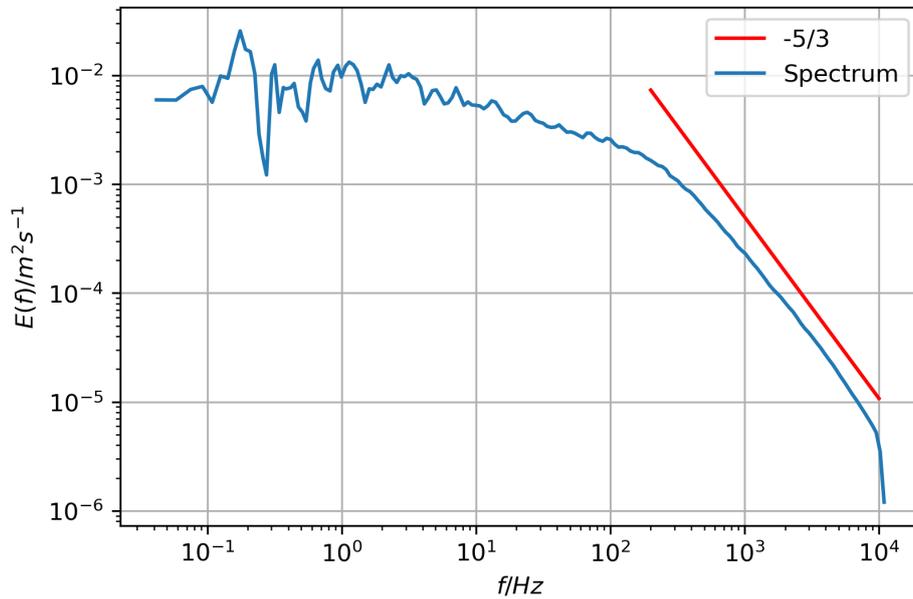
Figure 3. Power spectrum obtained from hot-wire measurements of the flow downstream of the regular grid in the frequency domain for the position $x/M = 11$.

3.4 Validation

Figure 4 shows the downstream evolution of k obtained theoretically with equation (23), experimentally using hot-wire measurements (section 3.1), and from simulation using the $k - \omega$ SST Menter 2003 model (see section 3.2) with both L and λ as boundary conditions at the inlet. First, we see that the theoretical equation is validated against experiments. Next, simulation

results obtained using both the Taylor micro-scale and the integral length as the boundary condition at the inlet are compared with equation (23). Here, we can clearly see that the simulation result obtained for the case where the Taylor micro-scale is used as the boundary condition matches very well with the theory. In contrast, when the integral length is used as boundary condition, the simulation results do not match the theory or the experimental results.

300 The justification for this observation comes directly from equation (23) where the derived 1d spatial evolution equation shows a direct dependence of the turbulent kinetic energy on the Taylor micro-scale.

It is also interesting to see how different $k-\omega$ models calculate the downstream evolution of k by using λ as the boundary condition. This is shown in figure 5. Here, we can see that the results from the $k-\omega$ SST Menter 2003, $k-\omega$ SST Menter 1994 and $k-\omega$ BSL Menter overlap with only a little deviation for the oldest $k-\omega$ series of the turbulence models, the $k-\omega$

305 Wilcox model.

This emphasizes the very important role of the choice of the turbulent length scale at the inlet as compared to the choice of the turbulent model. The following section showcases an instance of the digital twin's functionality, where an airfoil is subjected to testing in both the physical wind tunnel and the digital twin, with a subsequent comparison of the resulting loads.
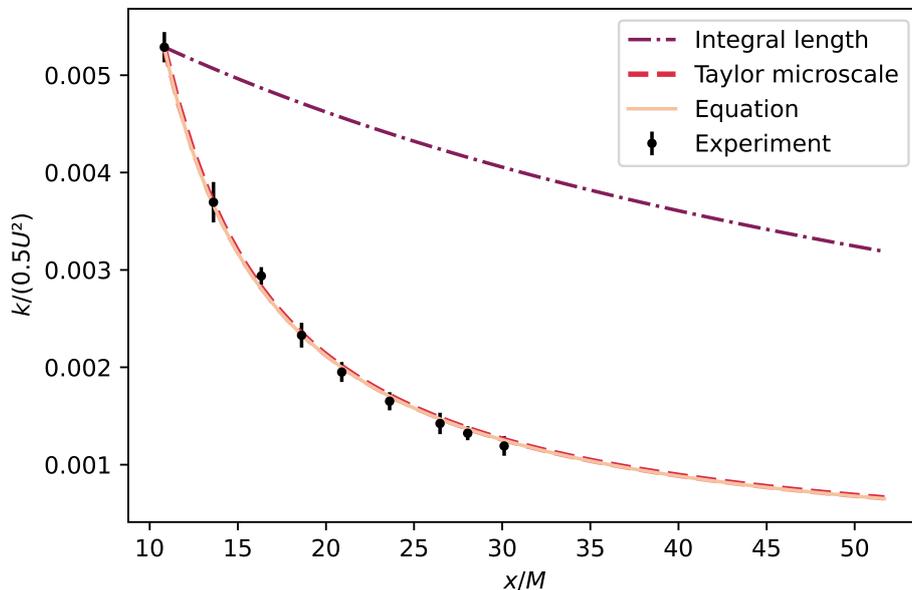
Figure 4. Comparison of the downstream evolution of $k/(0.5U^2)$ obtained from theory and experiments with simulations performed with integral length and Taylor micro-scale as the inlet boundary condition using the $k-\omega$ SST Menter 2003 model.
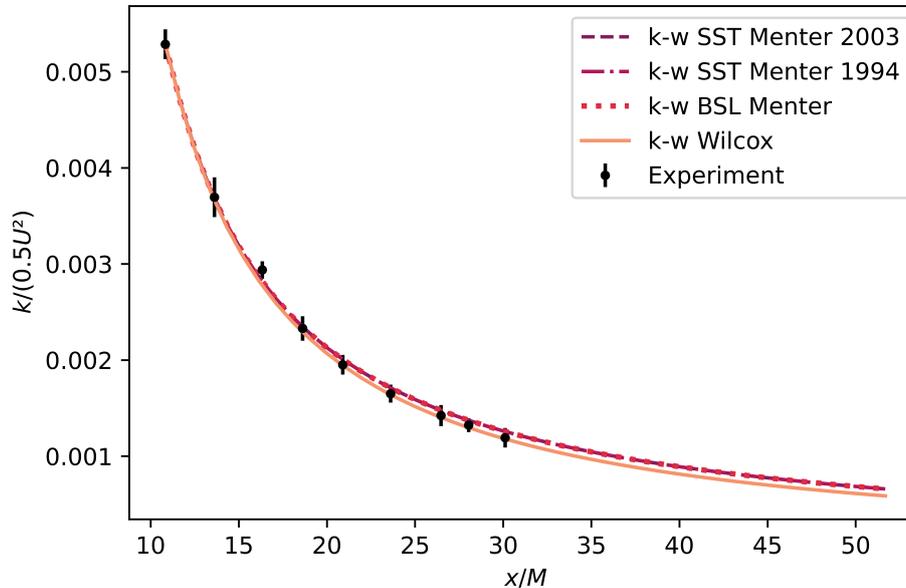
Figure 5. Comparison of the downstream evolution of $k/(0.5U^2)$ computed using different $k - \omega$ models

4 Example of the performance of the digital twin: testing an airfoil section of a wind turbine

The methodology to obtain a digital twin model of the experimented turbulent inflows is now validated. The present section is focusing on modeling the wind tunnel experiments to reproduce loads when a turbulent inflow is set. The same turbulent inflow as described in section 3.1 is used, which induces a homogeneous field with a turbulence intensity of 3%, measured at the airfoil position before its installation.

We are then introducing an airfoil model described in section 4.1.1, which is equipped with global load sensors (section 4.1.2) and local pressure sensors (section 4.1.3).

4.1 Experimental set-up

4.1.1 Airfoil

A 2d blade section was placed 1.79m downstream of the inlet where the flow field is homogeneous (see Neunaber and Braud (2020b)) in the wind tunnel described in section 3.1. The inlet velocity is $25\text{ms}^{-}1$. The airfoil shape was derived from scans of a 2MW wind turbine blade section, at 82% of its length (see also Neunaber et al. (2022)). It has been scaled-down to 1/10th of the original chord length, so that the chord length is $c = 0.125$ m and the chord-based Reynolds number is $Re_c = 2.0 \times 10^5$. The airfoil section closely resembles a NACA63-3-420 profile with a modified camber of 4% instead of 2% (see figure 6).
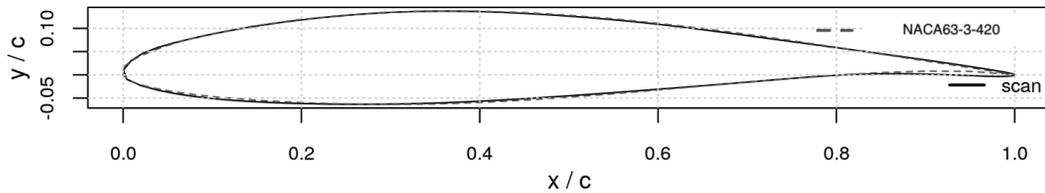
Figure 6. Blade section at 82% of the radius in comparison with a NACA63-3-420 profile with a modified camber of 4% instead of 2% (from Neunaber et al. (2022); published under CC BY-NC-ND 4.0 (License)).

The 2d blade section has been designed with multiple sensors to perform a 3d characterisation of the wall pressure over the airfoil surface, and future actuators and/or sensors can be implemented on the suction side (see figure 7). It was manufactured
325 from aluminium using a 3d metal printer to integrate channels for the pressure measurements. In total, four pressure scanners with sixteen channels each are used, and the locations of the pressure taps are given in section 4.1.2. The model is hollow and equipped with four covers on the suction side for access to the sensors. This also allows for the integration of actuators in the future. To perform simulations with the digital twin, it was important to check the shape of the airfoil for deviations and unevenness after manufacturing. Therefore, the down-scaled model has been scanned using the HandyScan 3d 700^{MC}
330 from CREAFORM that has an accuracy of 0.03mm. The scan was then compared to the initially designed shape that is used in simulations (see figure 8). At first, the covers of the 2d blade section had steps as high as 0.7mm, which was not accurate enough to produce experimental results that matched the simulations. These steps were significantly improved manually to an accuracy of less than 0.45mm, which was sufficient to match simulation results. It should be noted that for this inflow velocity, a TI of at least 3% was necessary to avoid low Reynolds number effects found in previous investigations (see Mishra et al.
335 (2022)).
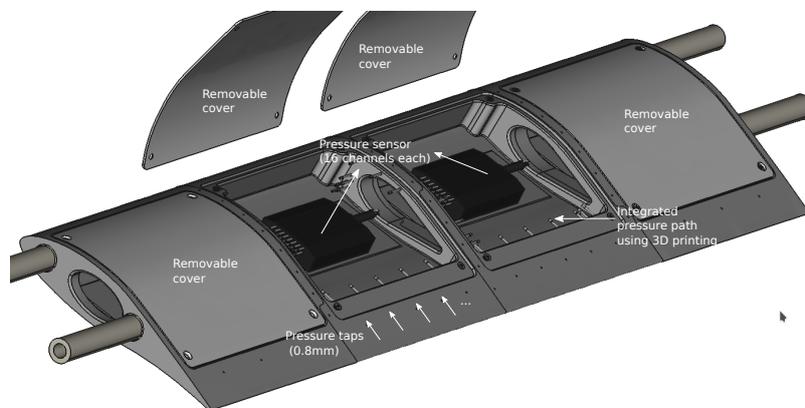
Figure 7. Computer Aided Design (CAD) drawing of the 3d printed 2d blade section mounted in the wind tunnel. The 2d blade section is made of aluminium. It is a hollow model that contains four pressure scanners with 16 channels each, which are connected to integrated pressure taps. The 2d blade section has four removable covers on the suction side to grant access to the pressure scanners.
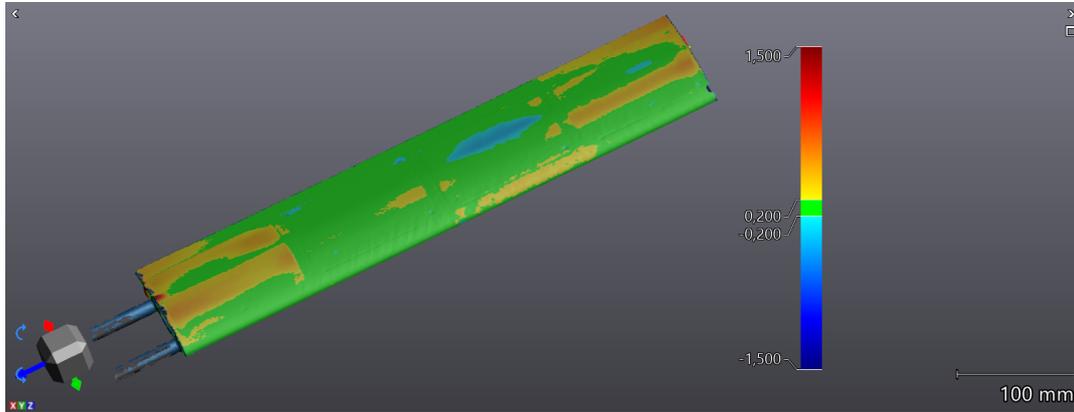
Figure 8. Illustration of the deviations (in mm) between the airfoil's original design shape and the shape achieved after the manufacturing process.

4.1.2 Local pressure sensors

The blade section is equipped with four differential pressure scanners from EvoScann® (P-Series) with 16 channels each that have a range of ±50mbar. The acquisition rate can be up to 1kHz, but it was limited to 100Hz for the present measurements as only steady quantities were targeted. These sensors were connected to wall pressure taps through channels integrated in the

340 blade designs, and tygon tubes. Three chord-wise lines of pressure taps were distributed (between the covers): at the mid-span, $z/c = 0$, and at $z/c = \pm 1$. The chord-wise distribution is identical for the three lines, and it is shown in figure 9 with exact positions in table 1. One span-wise line of pressure taps was added at $x/c = 0.88$, with pressure taps spaced by $0.16c$ from $z/c = -1$ to $z/c = 1$ and $0.25c$ otherwise.
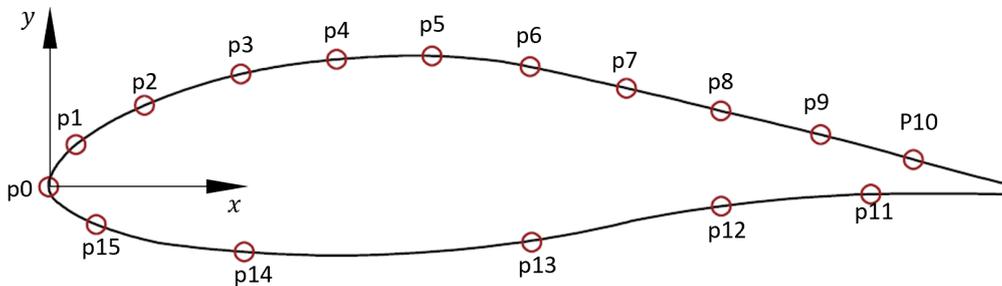
Figure 9. Chord-wise distribution of pressure ports around the airfoil - note that the axes are not scaled correctly.

Table 1. Position of pressure ports

Ports	p0	p1	p2	p3	p4	p5	p6	p7	p8	p9	p10	p11	p12	p13	p14	p15
x/c	0	0.03	0.1	0.2	0.3	0.4	0.5	0.6	0.7	0.8	0.9	0.85	0.7	0.5	0.2	0.05

4.1.3 Global load sensors

345   The airfoil was supported on two sides by load cells, cf. figure 10. The load cells work by the principle of strain measurement. Two load cells (one on each side) were used to measure the lift force (F_l), and two were used to measure the drag force (F_d). The load measurement system was calibrated in all directions (i.e., $+x$, $-x$, $+y$, and $-y$) using calibration weights between 500 g and 5000 g. The angle of attack was measured using a high-precision voltage-based angle sensor with a resolution of $0.035°$/mV. The signal from each load cell was collected at a sampling frequency of $f_s = 5000$Hz. The lift coefficient (C_l) and

350   the drag coefficient (C_d) were calculated using equations 32, and 33,

$$C_l = \frac{F_l}{\frac{1}{2}\rho A U^2},$$
(32)

$$C_d = \frac{F_d}{\frac{1}{2}\rho A U^2},$$
(33)

where ρ is the density of air, $A = 0.125\text{m} \times 0.5\text{m}$ is the airfoil's cross section, U is the inflow speed and ν is kinematic viscosity.
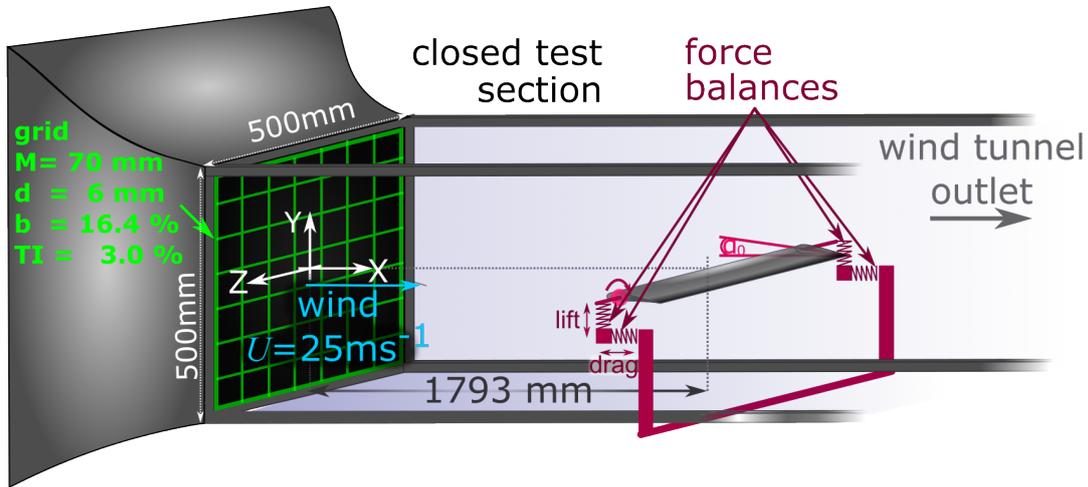
Figure 10. Wind tunnel setup for load measurements.

355   ### 4.2   Numerical setup for airfoil simulations

Figures 11, 12, and 13 present the 3d view, side view, and front view of the numerical domain (including mesh), respectively, for an angle of attack of the 2d blade section of α=0°. The mesh consists of 3 million cells, and figure 14 displays a close-up of the mesh around the airfoil. In this study, we only simulated the transverse half of the wind tunnel, as shown in figure 13. The shaded area in the figure was not simulated; instead, we applied a mirror boundary condition. The chord length of the airfoil

360   is 0.125m, which is the same as that used in the experiments. The airfoil is positioned at a downstream distance of 1.035m

from the inlet, as the simulation domain starts at the position of the first measurement point, where the inlet conditions are obtained and from where the turbulence decays. Therefore, the downstream position of the airfoil in the simulation is 0.758m less than that in the experiments, resulting in a downstream position of 1.035m.The inlet velocity is 25ms^{-1}, corresponding to $Re_c = 2.0 \times 10^5$ based on the chord length. The inlet turbulence intensity (TI) obtained from the hot-wire measurements

365 at $x/M = 11$, cf. section 3.4, is 4.4%, and the corresponding Taylor micro-scale is 2.54mm. In addition, we also use the integral length scale ($L = 25$mm) to investigate the impact of using the "wrong" length scale at the inlet. We applied a no-slip boundary condition on the airfoil with $y+ = 0.15$. At the outlet, we used a frozen pressure boundary condition. We imposed wall functions on the top wall (TW), bottom wall (BW), and side wall (SW) to avoid explicitly simulating the boundary layer. The $y+$ values for BW and TW are 50, and for the SW, it is 1.

370 We conducted unsteady 3d RANS simulations using the $k - \omega$ SST Menter 2003 model (see Menter et al. (2003)). To improve the computational efficiency and to accurately capture the flow downstream of the airfoil, we utilized an in-house adaptive grid refinement (AGR) methodology (see Wackers et al. (2012)). The total number of cells at the end of the simulation was approximately 16 million (see figure 15).
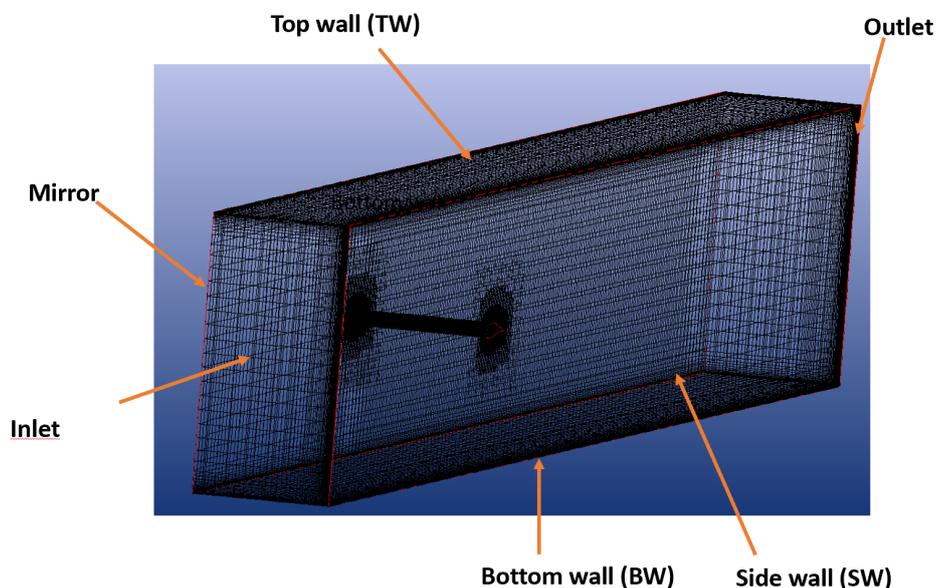
Figure 11. 3d mesh for the simulation of the flow over the airfoil (3 million cells)
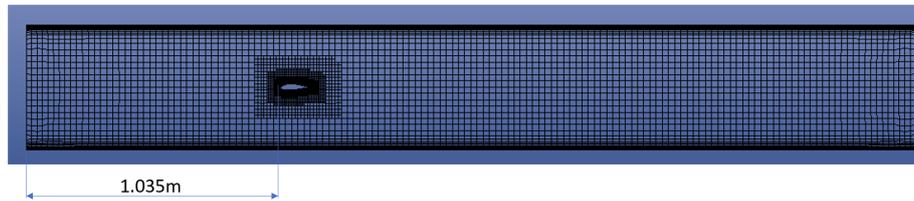
Figure 12. Side view of the mesh
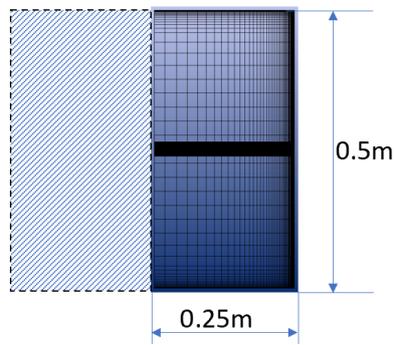
Figure 13. Front view of the mesh
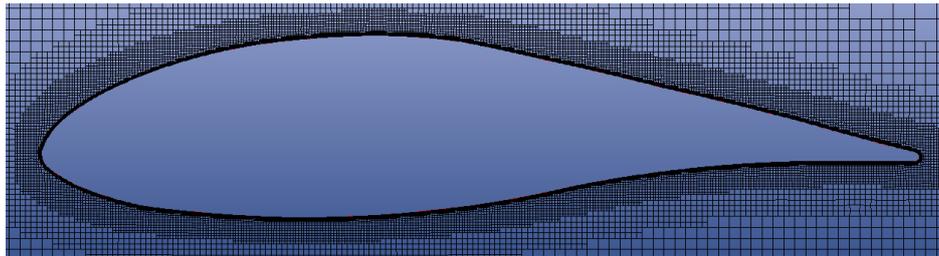
Figure 14. Mesh around the airfoil
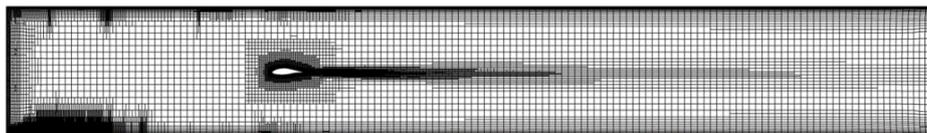
Figure 15. Side view of the mesh at end of simulation after adaptive grid refinement (16 million cells)

To obtain well-converged results for each angle of attack (AoA), we conducted 3d simulations using 400 cores on the IDRIS
375   Jeay Supercomputer. This process took almost 100 computing hours for each AoA.

4.3 Comparison between experiments and simulations

In the following sections, we present a comparison between the force coefficients and pressure coefficients obtained from the experiments and simulations.

4.3.1 Comparison of force coefficients obtained from digital twin and experiments

380 Figures 16 and 17 present a comparison between the C_l and C_d curves derived from wind tunnel experiments and their digital counterpart for a Reynolds number of 2.0×10^5. In one case, the inlet length scale is defined by λ, while in the other case, it is determined by the integral length scale. The experimental tests covered angles of attack (AoAs) ranging from $-5°$ to $24°$, whereas the simulations were conducted for AoAs between $0°$ and $20°$. The figures clearly demonstrate that our digital twin, utilizing λ as the inlet length scale, successfully replicates the force coefficients obtained in the original wind tunnel

385 experiments under turbulent inflow conditions. In contrast, when the integral length scale is used as the inlet length scale, higher lift values are observed across all AoAs (with the exception of $0°$), with the disparity increasing as the AoA increases. This increase in lift coefficient values in the simulations, utilising L as the boundary condition, can be attributed to the greater turbulence intensity experienced by the airfoil in the simulations compared to the experiments (cf., Abbott and Von Doenhoff (2012)). The inadequate representation of the evolution of the turbulent kinetic energy in the simulations subsequently affects

390 the representation of the turbulence intensity, resulting in notable deviations in the lift coefficients (C_l) between the simulations and experimental data.
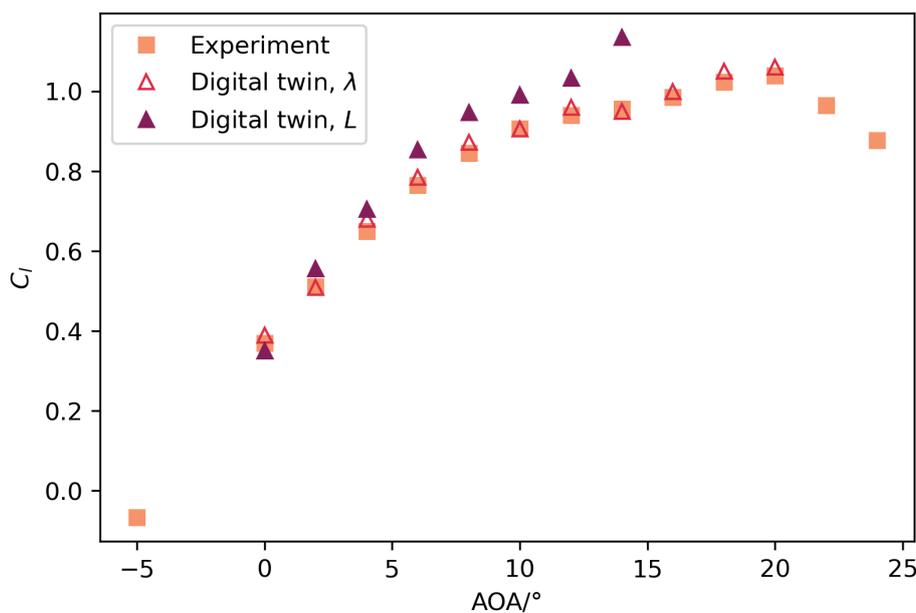
Figure 16. Comparison of C_l curves obtained from digital twin (using Taylor microscale (λ) and integral length (L)) and experiments for $Re_c = 2.0 \times 10^5$
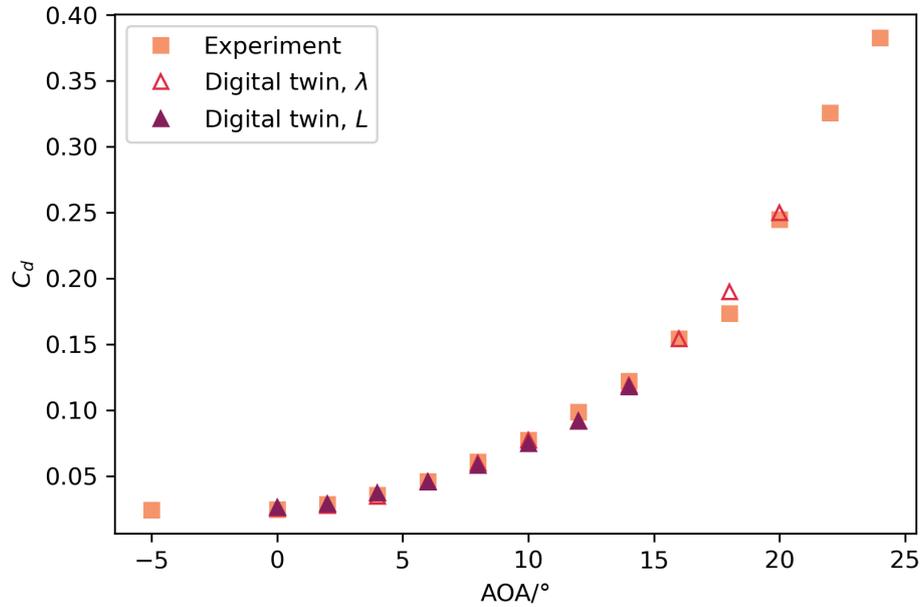
Figure 17. Comparison of C_d curves obtained from digital twin (using Taylor microscale (λ) and integral length (L)) and experiments for $Re_c = 2.0 \times 10^5$

In the next subsection, a comparison of the C_p obtained from simulations and experiments is made.

4.3.2 Comparison of C_p

Pressure measurements were performed over the surface of the airfoil, both experimentally and in the digital twin, for different
395   angles of attack (AoAs). Specifically, we compared the C_p values at AoAs of 0°, 4°, and 12°, encompassing a broad range of angles. For that we average over 3 spanwise positions ($z = 0$, $z = \pm 125$ mm) and plot the average. Figures 18, 19, and 20 depict the comparison between experimental and 3D simulation results. In these comparisons, we utilized both the Taylor length scale and the integral length scale as inlet conditions.

Overall, the simulation results closely align with the experimental results. However, there is a slight tendency towards higher
400   pressure on the pressure side, which could be attributed to difficulties in defining the reference pressure (which was measured inside the blade).

Moreover, the differences in C_p levels between using the Taylor length scale and the integral length scale become more pronounced as the angle of incidence increases. These differences primarily manifest on the suction side of the airfoil, particularly in the region of the leading-edge suction peak. Nevertheless, these differences are not significant for these local quantities.
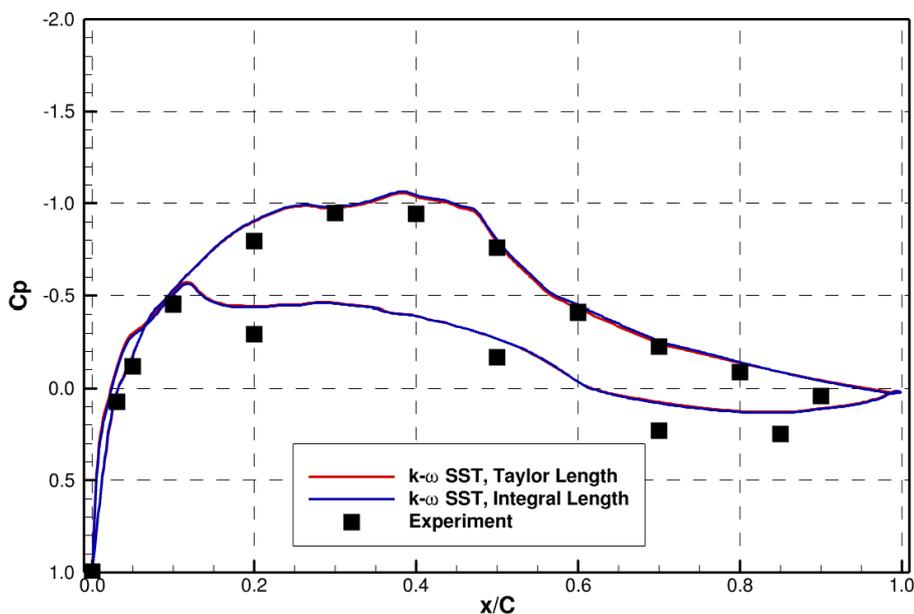
Figure 18. Comparative analysis of the C_p curve for AoA = 0° and $Re_c = 2.0 \times 10^5$, considering 3D simulations and experimental data. The comparison is conducted by averaging the results obtained from three spanwise positions ($z = 0$, $z = \pm125$ mm).
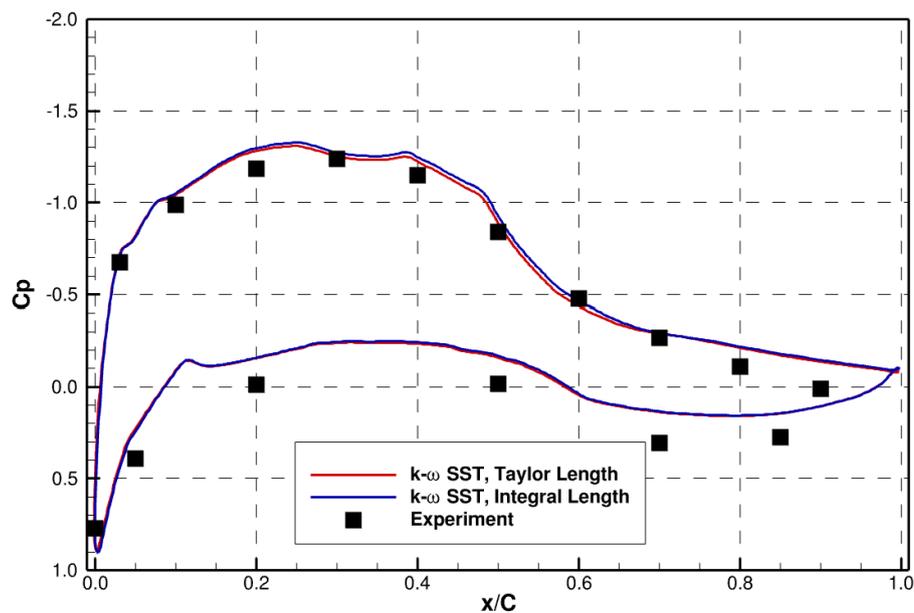
Figure 19. Comparative analysis of the C_p curve for AoA = 4° and $Re_c = 2.0 \times 10^5$, considering 3D simulations and experimental data. The comparison is conducted by averaging the results obtained from three spanwise positions ($z = 0$, $z = \pm125$ mm).
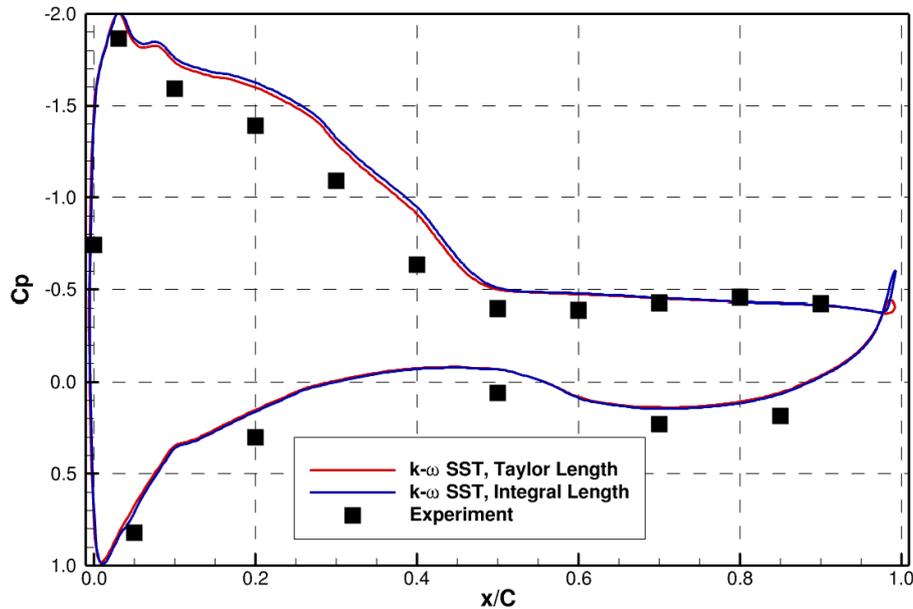
Figure 20. Comparative analysis of the C_p curve for AoA = 0° and $Re_c = 2.0 \times 10^5$, considering 3D simulations and experimental data. The comparison is conducted by averaging the results obtained from three spanwise positions ($z = 0$, $z = \pm125$ mm).

4.3.3 Comparison of the performance of 2d digital digital twin against 3d digital twin

This section provides a comparative study of force coefficients derived from both 2d and 3d digital twin simulations. Consistent initial and boundary conditions were maintained in both models. Figures 21 and 22 visually display the comparison for the lift and drag coefficient, respectively. The 2d outcomes are graphed for angles of attack between -5° and 16°, while the 3d results cover 0° to 16°.

The findings show a considerable correlation in the C_l values until an AoA of 12°. The exception to this is at 0° AoA, where the 3d model shows slightly elevated values compared to the 2d one. The 2d digital twin exhibits higher C_l values compared to the 3D digital twin for angle of attacks (AoAs) of 14° and above. The C_d values show a close match across all AoAs, with the exception of 16° AoA, at which point the 2d digital twin displays a higher C_d than its 3d counterpart.

The discrepancy in C_l values between the 3d and 2d digital twins can be traced back to the escalating significance of 3d effects at and above 14° AoAs, which are unaccounted for in the 2d model. As a result, if the emphasis is purely on force coefficients, the 2d digital twin can be used for low to moderately high AoAs due to its computational efficiency. For higher AoAs, where 3d effects are substantial, the more computationally demanding 3d digital twin is preferable. This strategic blend optimizes the use of the digital twin framework.
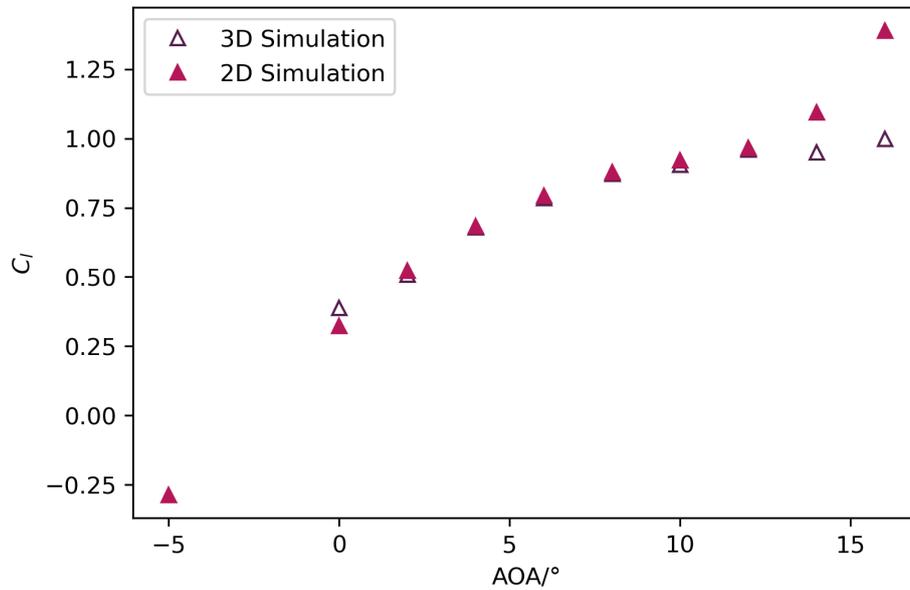
Figure 21. Comparison of C_l curve obtained from 3d digital twin and 2d digital twin for $Re_c = 2.0 \times 10^5$
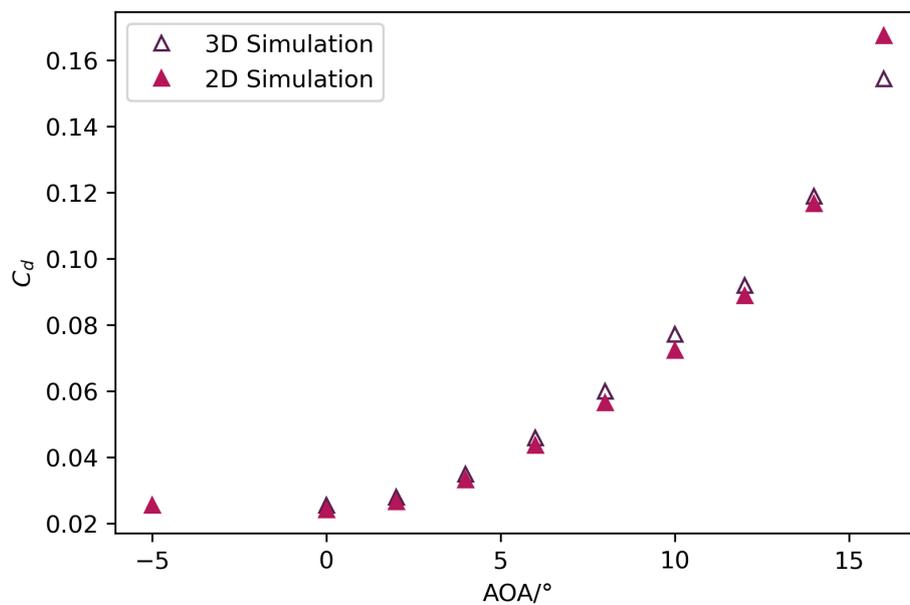
Figure 22. Comparison of C_d curve obtained from 3d digital twin and 2d digital twin for $Re_c = 2.0 \times 10^5$

5   Conclusions

420   We have successfully created a digital-twin of a wind tunnel with turbulent inflow conditions after creating a theoretical framework for the decay of the TKE, and we successfully expanded this digital-twin to perform 3d simulations of the impact of turbulent inflow on a 2d blade section. In the first part, a theoretical proof of the dependence of the downstream evolution of the turbulent kinetic energy on the Taylor micro-scale was developed for regular grid generated turbulent flows. It has then been demonstrated that the Taylor micro-scale is the correct turbulent length scale to be used as the boundary condition at the

425   inlet in RANS simulations for the accurate prediction of the downstream evolution of the turbulent kinetic energy. To validate our results, we compared the theoretical development with measurements performed downstream of a regular grid and RANS simulations using the $k - \omega$ SST Menter 2003 model. When the Taylor micro-scale (measured experimentally) is used as the inlet condition both for RANS simulations and for the theoretical equations, the turbulent kinetic energy measured experimentally is retrieved. In contrast, when the integral length scale is used as the inlet boundary condition, RANS simulations are far

430   from experiments and theory. Further, we compare the RANS results using several $k - \omega$ models with the Taylor micro-scale as the boundary condition, and the results are in good agreement with each other. This work thus demonstrates the validity of closure models in RANS equations to describe homogeneous, isotropic flows, as long as the Taylor micro-scale is used as one inlet boundary condition instead of the integral length scale.

Further, our results emphasise fundamental behaviours of grid generated turbulent flows:

435   1. The spatial evolution of the turbulent kinetic energy has a fundamental dependence on Taylor micro-scale, see equation (23).

2. For properly capturing the evolution of the turbulent kinetic energy either in space or time, the correct length scale given as the boundary condition is the Taylor micro-scale.

In the third part, we introduced an airfoil into the numerical wind tunnel and conducted 3d simulations at a chord-based

440   Reynolds number of $Re_c = 2.0 \times 10^5$. Our findings showed a nearly perfect agreement between the force coefficients obtained from experiments in the physical wind tunnel and those obtained from simulations in the numerical wind tunnel when using the Taylor micro-scale (λ) as the inlet length scale. This validates the suitability of the numerical wind tunnel for our purposes. In contrast, simulations using the integral length scale at the inlet resulted in significant differences in lift coefficients when compared to the experimental results. This demonstrates that accurately capturing the evolution of the turbulent kinetic energy

445   upstream of the airfoil is crucial for reproducing its aerodynamic behavior in numerical simulations. The comparison between the chord-wise pressure coefficients obtained from experiments and the digital twin revealed that they were similar on the suction side. However, significant differences in C_p values were observed on the pressure side. As the force coefficients obtained using load cells matched well with those obtained in the digital twin, this suggests that there may be room for improvement in the pressure measurement experiments. Moving forward, we plan to perform simulations at higher Reynolds numbers of

450   approximately $O(10^6)$ to further validate our numerical wind tunnel.

A comparison between 2d and 3d simulations also indicates that, if the emphasis is purely on force coefficients, the 2d digital twin can be used for low to moderately high AoAs due to its computational efficiency. For higher AoAs, where 3d effects are substantial, the more computationally demanding 3d digital twin is preferable. This strategic blend optimizes the use of the digital twin framework.

The authors advise the simulation community to be aware of the significant impact that the Taylor micro-scale (λ) has on the dissipation rate, which in turn affects the evolution of turbulent kinetic energy (TKE). Although different simulation codes may define length scales differently, they should all produce the same dissipation rate. To ensure consistency, the boundary condition for length scales in simulations should either be the Taylor micro-scale itself or a function of it (depending on definition used in a particular code). In the authors' study, the Taylor micro-scale is used directly as the boundary condition.

The methodology given in this paper is applicable for the limited case of regular grid generated turbulent flows. Thus, the next step is to study anisotropic flows. We will study the shear flows to understand the downstream and transverse evolution of the turbulent kinetic energy. The aim is to develop the evolution equation (23) which is 1D in nature into its 2d form. In the future, simulations will be performed for higher $Re_c \sim O(10^6)$ to validate our numerical wind tunnel for the higher Re_c.

Data availability. We are currently working on making the data presented here publicly accessible and will provide DOIs in a revised version of the manuscript.

Author contributions. RM developed the theoretical framework, carried out the simulations, acquired the aerodynamic data, performed the initial analysis and data investigation and wrote the original draft. IN acquired the hot-wire data and performed the initial analysis and data investigation. CB prepared the blade design with wall pressure measurements, followed its manufacturing and its shape corrections to match simulation results. CB acquired the funding. CB, EG, RM and IN developed the methodology. CB, EG and IN reviewed and edited the manuscript. EG supervised all the simulations.

Competing interests. The contact author has declared that neither they nor their co-authors have any competing interests.

Acknowledgements. This work is funded under French national project MOMENTA (grant no. ANR-19-CE05-0034) and the computations were performed using HPC resources from GENCI (Grand Equipement National de Calcul Intensif) (Grant-A0132A00129) which is gratefully acknowledged.

References

480   Abbott, I. H. and Von Doenhoff, A. E.: Theory of wing sections: including a summary of airfoil data, Courier Corporation, 2012.

Bailly, C. and Comte-Bellot, G.: Homogeneous and Isotropic Turbulence, in: Turbulence, pp. 129–177, Springer, 2015.

Bak, C.: Airfoil Design, pp. 95–122, Springer International Publishing, Cham, https://doi.org/10.1007/978-3-030-31307-4_3, 2022.

Batchelor, G. K. and Townsend, A. A.: Decay of isotropic turbulence in the initial period, Proceedings of the Royal Society of London. Series A. Mathematical and Physical Sciences, 193, 539–558, 1948.

485   Blackmore, T., Batten, W., and Bahaj, A.: Inlet grid-generated turbulence for large-eddy simulations, International Journal of Computational Fluid Dynamics, 27, 307–315, 2013.

Brunner, C. E., Kiefer, J., Hansen, M. O. L., and Hultmark, M.: Study of Reynolds number effects on the aerodynamics of a moderately thick airfoil using a high-pressure wind tunnel, Experiments in Fluids, 62, 2021.

Comte-Bellot, G. and Corrsin, S.: The use of a contraction to improve the isotropy of grid-generated turbulence, Journal of fluid mechanics, 490   25, 657–682, 1966.

Devinant, P., Laverne, T., and Hureau, J.: Experimental study of wind-turbine airfoil aerodynamics in high turbulence, Journal of Wind Engineering and Industrial Aerodynamics, 90, 689–707, 2002.

Djenidi, L.: Lattice-Boltzmann simulation of grid-generated turbulence, Journal of fluid mechanics, 552, 13–35, 2006.

Eça, L., Lopes, R., Vaz, G., Baltazar, J., and Rijpkema, D.: Validation exercises of mathematical models for the prediction of transitional 495   flows, in: Proceedings of 31st Symposium on Naval Hydrodynamics, 11th-16th September, Berkeley, 2016.

George, W. K.: The decay of homogeneous isotropic turbulence, Physics of Fluids A: Fluid Dynamics, 4, 1492–1509, 1992.

Germano, M., Piomelli, U., Moin, P., and Cabot, W. H.: A dynamic subgrid-scale eddy viscosity model, Physics of Fluids A: Fluid Dynamics, 3, 1760–1765, 1991.

Gilling, L., Sørensen, N., and Davidson, L.: Detached eddy simulations of an airfoil in turbulent inflow, in: 47th AIAA Aerospace Sciences 500   Meeting Including The New Horizons Forum and Aerospace Exposition, p. 270, 2009.

Hinze, J.: Turbulence, McGraw-Hill. ISBN 9780070290372, 1975.

Hultmark, M. and Smits, A. J.: Temperature corrections for constant temperature and constant current hot-wire anemometers, Measurement Science and Technology, 21, 105 404, 2010.

Kurian, T. and Fransson, J. H.: Grid-generated turbulence revisited, Fluid dynamics research, 41, 021 403, 2009.

505   Laizet, S. and Vassilicos, J. C.: DNS of fractal-generated turbulence, Flow, turbulence and combustion, 87, 673–705, 2011.

Laizet, S., Vassilicos, J., and Cambon, C.: Interscale energy transfer in decaying turbulence and vorticity–strain-rate dynamics in grid-generated turbulence, Fluid Dynamics Research, 45, 061 408, 2013.

Li, L. and Hearst, R. J.: The influence of freestream turbulence on the temporal pressure distribution and lift of an airfoil, Journal of Wind Engineering and Industrial Aerodynamics, 209, 104 456, https://doi.org/https://doi.org/10.1016/j.jweia.2020.104456, 2021.

510   License, C. C.: Attribution-NonCommercial-NoDerivatives 4.0 International (CC BY-NC-ND 4.0), https://creativecommons.org/licenses/by-nc-nd/4.0/, accessed: 2023-04-27.

Liu, L., Zhang, L., Wu, B., and Chen, B.: Numerical and Experimental Studies on Grid-Generated Turbulence in Wind Tunnel., Journal of Engineering Science & Technology Review, 10, 2017.

Menter, F. R.: Two-equation eddy-viscosity turbulence models for engineering applications, AIAA journal, 32, 1598–1605, 1994.

515   Menter, F. R., Kuntz, M., and Langtry, R.: Ten years of industrial experience with the SST turbulence model, Turbulence, heat and mass transfer, 4, 625–632, 2003.

Miller, M. A., Kiefer, J., Westergaard, C., Hansen, M. O. L., and Hultmark, M.: Horizontal axis wind turbine testing at high Reynolds numbers, Physical Review Fluids, 4, 110 504, https://doi.org/10.1103/PhysRevFluids.4.110504, 2019.

Mishra, R., Neunaber, I., Guilmineau, E., and Braud, C.: Wind tunnel study: is turbulent intensity a good candidate to help in bypassing low
520   Reynolds number effects on 2d blade sections?, in: Journal of Physics: Conference Series, vol. 2265, p. 022095, IOP Publishing, 2022.

Mydlarski, L. and Warhaft, Z.: On the onset of high-Reynolds-number grid-generated wind tunnel turbulence, Journal of Fluid Mechanics, 320, 331–368, 1996.

Nagata, K., Suzuki, H., Sakai, Y., Hayase, T., and Kubo, T.: Direct numerical simulation of turbulent mixing in grid-generated turbulence, Physica Scripta, 2008, 014 054, 2008.

525   Neunaber, I. and Braud, C.: Aerodynamic behavior of an airfoil under extreme wind conditions, in: Journal of Physics: Conference Series, vol. 1618, p. 032035, IOP Publishing, 2020a.

Neunaber, I. and Braud, C.: First characterization of a new perturbation system for gust generation: the chopper, Wind Energy Science, 5, 759–773, 2020b.

Neunaber, I., Danbon, F., Soulier, A., Voisin, D., Guilmineau, E., Delpech, P., Courtine, S., Taymans, C., and Braud, C.: Wind tunnel study
530   on natural instability of the normal force on a full-scale wind turbine blade section at Reynolds number $4.7 \cdot 10^6$, Wind Energy, 25, 1332–1342, https://doi.org/https://doi.org/10.1002/we.2732, 2022.

Nicoud, F., Toda, H. B., Cabrit, O., Bose, S., and Lee, J.: Using singular values to build a subgrid-scale model for large eddy simulations, Physics of fluids, 23, 085 106, 2011.

Nietiedt, S., Wester, T. T. B., Langidis, A., Kröger, L., Rofallski, R., Göring, M., Kühn, M., Gülker, G., and Luhmann, T.: A Wind Tunnel
535   Setup for Fluid-Structure Interaction Measurements Using Optical Methods, Sensors, 22, https://doi.org/10.3390/s22135014, 2022.

Panda, J., Mitra, A., Joshi, A., and Warrior, H.: Experimental and numerical analysis of grid generated turbulence with and without mean strain, Experimental thermal and fluid science, 98, 594–603, 2018.

Rieth, M., Proch, F., Stein, O., Pettit, M., and Kempf, A.: Comparison of the Sigma and Smagorinsky LES models for grid generated turbulence and a channel flow, Computers & Fluids, 99, 172–181, 2014.

540   Sicot, C., Aubrun, S., Loyer, S., and Devinant, P.: Unsteady characteristics of the static stall of an airfoil subjected to freestream turbulence level up to 16%, Experiments in Fluids, 41, 641–648, https://doi.org/10.1007/s00348-006-0187-9, 2006.

Smagorinsky, J.: General circulation experiments with the primitive equations: I. The basic experiment, Monthly weather review, 91, 99–164, 1963.

Speziale, C. G. and Bernard, P. S.: The energy decay in self-preserving isotropic turbulence revisited, Journal of Fluid Mechanics, 241,
545   645–667, 1992.

Stewart, R. W. and Townsend, A. A.: Similarity and self-preservation in isotropic turbulence, Philosophical Transactions of the Royal Society of London. Series A, Mathematical and Physical Sciences, 243, 359–386, 1951.

Suzuki, H., Nagata, K., Sakai, Y., and Hayase, T.: Direct numerical simulation of turbulent mixing in regular and fractal grid turbulence, Physica Scripta, 2010, 014 065, 2010.

550   Torrano, I., Tutar, M., Martinez-Agirre, M., Rouquier, A., Mordant, N., and Bourgoin, M.: Comparison of experimental and RANS-based numerical studies of the decay of grid-generated turbulence, Journal of Fluids Engineering, 137, 2015.

Veers, P., Dykes, K., Lantz, E., Barth, S., Bottasso, C. L., Carlson, O., Clifton, A., Green, J., Green, P., Laird, D., V. Lehtomäki, J. K. L., Manwell, J., M. Marquis, C. M., Moriarty, P., Munduate, X., Muskulus, M., Naughton, J., Pao, L., Paquette, J., Peinke, J., Robertson, A., Rodrigo, J. S., Sempreviva, A. M., Smith, J. C., Tuohy, A., and Wiser, R.: Grand challenges in the science of wind energy, Science, 366, 2019.

Versteeg, H. and Malalasekera, W.: An introduction to Computational Fluid Dynamics Prentice Hall, 1995.

Wackers, J., Deng, G., Leroyer, A., Queutey, P., and Visonneau, M.: Adaptive grid refinement for hydrodynamic flows, Computers & Fluids, 55, 85–100, 2012.

Wei, N. J., Kissing, J., Wester, T. T. B., Wegt, S., Schiffmann, K., Jakirlic, S., Hölling, M., Peinke, J., and Tropea, C.: Insights into the periodic gust response of airfoils, Journal of Fluid Mechanics, 876, 237–263, https://doi.org/10.1017/jfm.2019.537, 2019.

Wester, T. T., Kröger, L., Langidis, A., Nietiedt, S., Rofallski, R., Goering, M., Luhmann, T., Peinke, J., and Gülker, G.: Fluid-Structure Interaction Experiments on a Scaled Model Wind Turbine Under Tailored Inflow Conditions Using PIV and Photogrammetry, in: 20th International Symposium on Application of Laser and Imaging Techniques to Fluid Mechanics, July 11th-14th 2022, Lisbon, Portugal, 2022.

Wilcox, D. C.: Reassessment of the scale-determining equation for advanced turbulence models, AIAA journal, 26, 1299–1310, 1988.

Zhou, Y. and Speziale, C. G.: Advances in the fundamental aspects of turbulence: energy transfer, interacting scales, and self-preservation in isotropic decay, Applied Mechanics Reviews, 51, 267–301, 1998.